# Nanoscale

Accepted Manuscript

This is an *Accepted Manuscript*, which has been through the Royal Society of Chemistry peer review process and has been accepted for publication.

Accepted Manuscripts are published online shortly after acceptance, before technical editing, formatting and proof reading. Using this free service, authors can make their results available to the community, in citable form, before we publish the edited article. We will replace this *Accepted Manuscript* with the edited and formatted *Advance Article* as soon as it is available.

You can find more information about *Accepted Manuscripts* in the **Information for Authors**.

ROYAL SOCIETY OF CHEMISTRY

www.rsc.org/nanoscale

Performance study of magnesium-sulfur battery using graphene based sulfur composite as cathode electrode and a non-nucleophilic Mg electrolyte

B. P. Vinayan *[a]*, *Zhirong Zhao-Karger* *[b]*, *Thomas Diemant* *[c]*, *Venkata Sai Kiran Chakravadhanula* *[a,b,d]*, *Nele I. Schwarzburger* *[a]*, *Musa Ali Cambaz* *[a]*, *R. Jürgen Behm* *[a,c]*, *Christian Kübel* *[a,b,d]*, *Maximilian Fichtner* *[a,b]*

[a]Helmholtz Institute Ulm for Electrochemical Energy Storage (HIU), Helmholtzstr. 11, D-89081 Ulm, Germany

[b]Institute of Nanotechnology, Karlsruhe Institute of Technology (KIT), P.O. Box 3640, D-76021 Karlsruhe

[c] Institute of Surface Chemistry and Catalysis, Ulm University, Albert-Einstein-Allee 47, D-89081 Ulm, Germany

[d] Karlsruhe Nano Micro Facility, Karlsruhe Institute of Technology, D-76344 Eggenstein-Leopoldshafen, Germany

Phone: +49 (0)731 50 34201, Fax: +49 (0)731 50 34299,

maximilian.fichtner@kit.edu, vinayan.parambath@kit.edu

Abstract

Here we report for the first time the development of a Mg rechargeable battery using graphene-sulfur nanocomposite as cathode, a Mg-carbon composite as anode and a non-nucleophilic Mg electrolyte in tetraglyme solution as electrolyte. The graphene-sulfur nanocomposites are prepared through a new pathway by the combination of thermal and chemical precipitation methods. The Mg/S cell delivers a higher reversible capacity (448 mAh g^{-1}), longer cyclability (236 mAh g^{-1} at the end of 50th cycle) and better rate capability than previously described cells. The dissolution of Mg polysulfides to the anode side was studied by X-ray photoelectron spectroscopy. The use of a graphene-sulfur composite cathode electrode, with the properties of high surface area, porous morphology, very good electronic conductivity and presence of oxygen functional groups, along with a non-nucleophilic Mg electrolyte give the improved battery performance.

Keywords*: Rechargeable magnesium battery, sulfur, reduced graphene oxide, non-nucleophilic electrolyte, polysulfides, oxygen functional groups*.

Nanoscale Accepted Manuscript

1. Introduction

Rechargeable magnesium (Mg) batteries have been proposed for electrochemical energy storage of renewable energy and realization of electric vehicles because of the inherent merits associated with Mg such as natural abundance, operational safety and high volumetric capacity. Among different kind of alkaline/alkaline earth metal anodes, magnesium (Mg) has the highest theoretical volumetric capacity (3,832 mAh cm^{-3}) and a high negative reduction potential of -2.356 V *versus* normal hydrogen electrode (NHE). For comparison, the graphite anodes presently used in lithium ion batteries (LIBs) have a volumetric capacity of 777 mAh cm^{-3} only.[1] Mg as anode material can be considered as safer electrode in liquid electrolytes because it is not forming dendrites as compared to lithium.[2] Theoretical calculations show that Mg favors the growth of smooth surfaces as compared to Li and Na due to its lower diffusion barriers and higher-coordinated configurations.[3] In addition, the raw material for Mg is cheaper than lithium and its compounds are usually non-toxic.

Among the different types of cathode materials, sulfur (S) would be a promising cathode for Mg based rechargeable batteries because of its high theoretical capacity (1,671 mAh g^{-1} or 3,459 mAh cm^{-3}) and natural abundance. The combination of a Mg anode and a sulfur cathode yields a theoretical volumetric energy density of 3200 Wh l^{-1} as compared to 2800 Wh l^{-1} for a lithium-sulfur battery.[1, 4] However, a number of issues have to be addressed for the realization of a Mg/S rechargeable battery system. A challenge, which has limited the development of rechargeable Mg/S battery, was the availability of suitable electrolytes with high ionic conductivity, wherein Mg could be deposited reversibly.[5] This is mainly because

of the strong electrophilic nature of sulfur, which demands a non-nucleophilic electrolyte. Muldoon *et al.* succeeded to develop a non nucleophilic electrolyte by the addition of $AlCl_3$ to the THF solution of hexamethyldisilazide magnesium chloride and tested the first Mg/S battery cell for two cycles with discharge capacities of 1200 mAh g^{-1} and 394 mAh g^{-1}, respectively, at a discharge voltage of around 1 V.[1] Recently, Zhao-Karger *et al.* reported a non-nucleophilic electrolyte for Mg/S battery based on a non-nucleophilic base of magnesium-bis(hexamethyldisilazide) $[(HMDS)_2Mg]$ transmetallated with $AlCl_3$ as Lewis acid (1:2 molar ratio) and dissolved the reaction product in different ethereal solvents.[6] Using these electrolytes, the discharge potential of Mg/S battery was improved up to 1.65 V, which is close to the thermodynamic value of voltage (~1.7 V).[7]

The first studies on Mg/S rechargeable battery indicated issues like polarization effect during charging, low cyclic stability, initial capacity fading and polysulfide dissolution, analogous to the Li/S battery system.[8, 9] In Li/S batteries, the soluble polysulfides lead to self-discharge and a degradation of the cell.[10, 11] The electrical insulating property of the sulfur material is another problem that gives low electronic charge transfer to the current collectors. To address some of these issues it is necessary to design a composite of nano dispersed active sulfur material in a proper carbon host matrix. The carbon host material needs to have (a) a strong chemical anchoring of sulfur and subsequently formed polysulfides, (b) a high electrical conductivity, (c) a mechanically stable framework to uphold the strain generated by the volume changes of the sulfur during cycling, (d) easy access of liquid electrolyte to the sulfur active material, and (e) small pores without big openings to accommodate polysulfides. Among different types of carbon nanomaterials, graphene (G) based nanostructures have emerged as preferred materials for energy storage applications due to their unique properties

such as large surface area, high charge mobility, excellent electronic and thermal conductivity, high mechanical strength and good chemical stability.[12-14]

In this paper, we have investigated the cell performance and working mechanism of a reduced graphene oxide/sulfur nanocomposite cathode material in a Mg/S rechargeable battery system using a non-nucleophilic Mg electrolyte. The rGO-sulfur nanocomposite has been prepared by a combination of thermal and chemical precipitation methods.

2. Experimental

2.1 Material synthesis

2.1(a) Preparation of sulfur-reduced graphene oxide nanocomposite (S-rGO)

Reduced graphene oxide (rGO) was prepared by the thermal exfoliation of graphite oxide (GO) at 400 ºC in argon gas atmosphere, where GO was initially synthesized by Hummer's method.[15] Sodium polysulfide (Na_2S_x) solution was prepared by dissolving 1.29 g of sodium sulfide powder (Na_2S, Anhydrous, Alfa Aesar) in 50 ml of Millipore water and subsequently adding 1.6 g of sublimed sulfur (99.5 %, Alfa Aesar) to this solution and dispersing well by ultra-sonication and stirring. The change in the color of the solution from yellow to orange during the dissolution of sulfur indicates the formation of sodium polysulfide solution. Next, 0.2 g of rGO was dispersed in 200 ml of deionized water by ultra-sonication and Na_2S_x solution was added drop wise to rGO solution using a burette during stirring. rGO-Na_2S_x solution was continuously stirred for the next 24 h. Then, 200ml of 2M formic acid (HCOOH, ≥96%, Sigma-Aldrich) was slowly added to the rGO-Na_2S_x solution using a burette while stirring and allowed to stir for additional 6 h. The final sample was filtered, washed and dried at 50 ºC in

vacuum for 12 h. Then this sample was heat-treated initially at 160 ºC for 4 h. and further heated at 300 ºC for 1 h in argon atmosphere.

2.1(b) Preparation of magnesium-carbon composite (Mg-C)

Magnesium powder (Magnesium powder, 325 mesh, 99.8%, Alfa Aesar) and conductive carbon black (TIMCAL C.NERGY SUPER C65) were ball milled together in the weight ratio (80:20) using a planetary ball-mill (Fritsch PULVERISETTE 6) with 80 ml silicon nitride vial and silicon nitride balls in argon atmosphere at 200 rpm for 12 h.

2.1(c) Synthesis of electrolyte

The synthesis procedure was carried out in an argon filled glove box and explained in detail in our previous paper.[6] In brief, magnesium-bis(hexamethyldisilazide) [97 %, Sigma-Aldrich] (1.24 g) was dissolved in 4 mL of tetraglyme [anhydrous, ≥99 %, Aldrich] in a glass vial. Subsequently anhydrous $AlCl_3$ [99.999 %, Sigma-Aldrich] (0.96 g) was slowly added to this solution and stirred for the next 36 h at room temperature. After that $MgCl_2$ [anhydrous, Sigma-Aldrich], (0.343 g) was added to the solution and continuously stirred for 48 h.

2.2 Characterization of materials

The X-ray diffraction (XRD) measurements were conducted in a Stadi P diffractometer (STOE & Cie) with a MYTHEN detector using the Cu K_α X-ray source. Raman measurements were carried out with a confocal Raman microscope (InVia, RENISHAW) in the spectral range 800 – 2000 cm^{-1} using a 532 nm laser excitation source. Thermo gravimetric analysis (TGA) of the samples were carried out along with

differential scanning calorimetry (DSC) using a Setaram thermal analyzer SENSYS evo instrument. The measurements were conducted from room temperature to 600 ºC under helium flow (20 ml/min) with a heating rate of 10 ºC min^{-1}. To identify different functional groups within the samples, FTIR experiments were performed using FTIR spectrometer (Spectrum Two, PerkinElmer) in the spectral range of 500-4000 cm^{-1}.

The morphological studies of the samples were studied using scanning electron microscopy (SEM, LEO GEMINI 1550 VP) and transmission electron microscopy (TEM). TEM characterization of the nanocomposite was carried out using an aberration corrected FEI Titan 80-300 operated at 80 kV and 300 kV equipped with a Gatan imaging filter (Tridiem 863). For (S)-TEM measurements, samples were prepared by dispersing a small amount of powder directly onto holey carbon Au grids (Quantifoil).

The chemical state of the sample surfaces was determined by X-ray Photoelectron Spectroscopy (XPS) measurements using monochromatized Al K$_\alpha$ (1486.6 eV) radiation (PHI 5800 MultiTechnique ESCA System, Physical Electronics). The measurements were done with a detection angle of 45°, using pass energies at the analyzer of 93.9 and 29.35 eV for survey and detail spectra, respectively. The samples were neutralized with electrons from a flood gun (current 3 µA) to compensate for charging effects at the surface. For binding energy calibration the C(1s) peak of the graphene was set to 284.5 eV. To avoid surface contamination, the samples were transferred in inert gas atmosphere to the sample load lock of the XPS system.

2.3 Electrochemical measurements

The cathode electrodes were made by mixing 75 wt. % of S-*r*GO with 10 wt. % polyvinylidenefluoride (PVDF, Kynar) binder and 15 wt. % Super P carbon, using N-methyl-2-pyrrolidinone (NMP, Sigma-Aldrich) as solvent. The slurry was uniformly coated over an Inconel 625 current collector disk (10 mm diameter) and dried at 60 °C for 24 h to remove the solvent. Electrochemical measurements were conducted using a Swagelok type cell with S-*rGO* as cathode electrode, Mg-carbon composite pellets (10 mm) as anode electrode, Celgard 2500 as the separator, and a non-nucleophilic electrolyte. The whole assembling of the cells was conducted inside an argon filled glovebox (MBRAUN) with recirculation unit. Galvanostatic charge–discharge measurements were performed using an electrochemical workstation (ARBIN INSTRUMENTS) between 2.5 and 0.5 V *vs.* Mg^{2+}/Mg at room temperature.

3. Results and Discussion

Fig. 1 shows a scheme of the impregnation of sulfur atoms to the reduced graphene oxide (*r*GO) structures, where *r*GO was prepared by the thermal exfoliation of graphite oxide (GO) at 400 °C in argon atmosphere. Since the exfoliation of GO is done at moderate temperature, the process retains some amount of various oxygen functional groups such as hydroxyl, epoxide, carbonyl, and carboxyl groups over the surface of the graphene layers. The presence of various oxygen functional groups over rGO was later confirmed by FTIR and XPS characterization techniques (see the discussion below). Sulfur was dispersed over *r*GO by

chemical precipitation method using sodium polysulfide (Na_2S_x) as the sulfur source and formic acid (HCOOH) as the reducing agent in aqueous media. Initial heat treatment of this composite at 160 °C for 4 h causes the melting of sulfur and subsequent diffusion over the layers and into pores of rGO. Further heat treatment of this composite at 300 °C for 1 h helps to remove the non-adsorbed sulfur particles from the graphene surface and also to control the sulfur loading within the composite. During this process, the sulfur is dispersed uniformly over graphene layers because of (a) its 2 dimensional high surface area morphology, (b) its porous structure, and (c) the presence of various oxygen functional groups over rGO.

The XRD patterns of *rGO*, sublimed sulfur and S-*rGO* nanocomposite are shown in Fig. 2. The broad peak of *rGO*, ranging from 14° to 30° is an indication of the loss of crystallinity through the (002) graphitic plane and formation of stacked layers of graphene. After thermal exfoliation, the (002) *d* spacing of rGO was increased to 3.55 Å as compared to the starting graphite (*d* = 3.35 Å).[16] XRD of sublimed sulfur gives the main peaks centered at $2\theta = 23.4°$ and 28.0°, and matches well with the (222) and (040) reflections of the *Fddd* orthorhombic phase (JCPSD no. 08-0247). The sharp and strong diffraction peaks of sublimed sulfur confirm the well-defined crystal structure. The XRD pattern of the S-*rGO* nanocomposite did not exhibit any sulfur peaks, which is probably due to the confinement of sulfur within the pores of *rGO*.

Raman spectroscopy is a powerful analytical tool for carbon materials to evaluate the degree of graphitic order and doping.[17] *rGO* and S-*rGO* samples showed two main peaks corresponding to G and D bands as shown in Fig. 3. The G band is due to the Raman active E_{2g} mode and measures the crystallinity of a carbon material. The D band represents the

breathing mode of the sp^2 ring of the graphene layers, which is sensitive to different kinds of structural and heteroatom doping defects.[17] The intensity ratio between D and G band, (I_D/I_G) is usually used to measure the defect density in the carbon nanostructures. I_D/I_G ratio for *rGO* and S-*rGO* samples were 0.85 and 1.01, respectively, and the increased I_D/I_G ratio for S-*rGO* sample is ascribed to an enhanced structural distortion caused by S doping within the graphene lattice. The peak positions for the G band in *rGO* and S-*rGO* samples were at 1603 cm^{-1} and 1590 cm^{-1}, i.e., a downward shift of 13 cm^{-1} was observed after S doping. Similar downward shift of the G band has been reported already for sulfur and nitrogen doped graphene samples.[18, 19] These studies showed that adsorption of molecules over graphene with electron donating groups can lead to a downshifting and stiffening of the G band.[20]

TGA and DSC data of rGO and S-rGO are shown in Fig. 4. Sublimed sulfur is in the form of S_8 rings and converts into a linear polymeric bi-radical molecule (-S-S_6-S-) in the temperature range of about ~ 160 °C by an endothermic reaction called λ-transition.[21] The DSC thermogram of elemental sulfur mainly comprises three endothermic signals: the first one corresponds to the α → β transition of the sulfur at around 100 °C, the second is the melting of the β-sulfur which starts at ~ 120 °C, and the third is the λ-transition which starts at ~ 160 °C. The sulfur within the S-rGO nanocomposite was completely sublimated at ~ 330 °C. TGA confirmed the ~ 49 wt. % sulfur loading within the nanocomposite.

The presence of different oxygen functional groups and the bonding of sulfur with oxygen within rGO and S-rGO samples were verified by FTIR (Fig. 5, Fig. S1: supporting information). In the FTIR spectrum of S-rGO, the strong bands at ~ 3670 cm^{-1} (O–H stretch),

2986-2901 cm^{-1} (C–H stretch), ~ 1405 cm^{-1} (C-H bends) and 1300-1150 cm^{-1} (C-O stretch of

–COOH or S=O stretch of sulfones) suggest the existence of hydroxyl and carboxyl

functional groups. The strong peak in the range of 1130-1000 cm^{-1} contains the contribution

from S=O stretch (sulfoxide) and C-O stretch (alcohol group). Moreover, the bands at 950-

800 cm^{-1} and ~ 552 cm^{-1} indicate the bond formation of S-OR (esters) and S-S (disulfide),

respectively.

Bright-field TEM (Fig. 6 (a)) and SEM (Fig. S2: supporting information) images of the S-

rGO illustrate the wrinkled thin layered morphology of the sample.[22] Energy filtered

transmission electron microscopy (EFTEM) elemental mapping of the marked area of the

TEM image (Fig. 6 (a)) using C-K edge and S-L edges are shown in Fig. 6 (b) & (c),

respectively. From these elemental maps, it is evident that there is uniform distribution of

sulfur over the graphene layers. The same can also be observed from the scanning

transmission electron microscopy (STEM) image (Fig. 6 (d)), where no variations in z-

contrast are observed. Fig. 6 (e) shows a bright-field TEM image of S-rGO accompanied with

the corresponding selected area diffraction (SAED) pattern. The strong texturing observed

from the SAED pattern is from the wrinkled morphology of the sample. The *d*-value of the

(002) graphitic plane measured from the SAED pattern is ~ 3.54 Å, which is comparable to

the XRD results for S-rGO (cf. Fig. 2). The high resolution TEM micrograph (Fig. 6 (f)) of S-

rGO illustrates stacked graphene layer morphology of the sample. The presence of carbon,

oxygen and sulfur within the S-rGO nanocomposite was further confirmed by energy

11

dispersive X-ray spectroscopy (Fig. 6 (g)) and electron energy loss spectroscopy (Fig. 6 (h)), corresponding to the area marked in the STEM image of Fig. 6 (d).

To investigate the chemical bonding between different elements such as carbon, oxygen and sulfur in more detail, X-ray photoelectron spectroscopy (XPS) measurements were carried out for *rGO* and S-*rGO* samples. The high resolution O1s spectrum of *rGO* (Fig. 7 (a)) shows two peaks, which can be attributed to C-O (533.1 eV) and C=O (531.3 eV) species, respectively.[23] After sulfur addition (S-*rGO*, Fig. 7 (b)), another peak appears at 531.6 eV, which can be attributed to the formation of S=O bonds.[23] These bond formations let the sulfur immobilize on the *rGO* surfaces during battery charge/discharge. For example, recent studies of a Li/S battery had shown that oxygen functional groups on carbon support can bond with polysulfides and thus mitigate the diffusion to the anode side.[24, 25] The high-resolution C1s spectrum of *rGO* (Fig. 7 (c)) also illustrates the presence of C-O (epoxide etc., at 286.5 eV) and C=O (289.2 eV) bond formation on the graphene substrate, the peaks at 284.5 eV and 285.2 eV are assigned to graphene and C-H (and /or sp³-hybridized C-C) groups, respectively. For the S-*rGO* sample, an increase of the intensity of the component at 285.2 eV and a decrease of the two peaks at higher binding energy (which we attribute to carbon with oxygen bonding) is observed. The binding energy (BE) of carbon with a C-S bond is very close to that with a C-H (or sp³-hybridized C-C) bond,[26, 27] the increase of the peak at 285.2 eV in the spectrum of the S-*rGO* is therefore assigned to sulfur deposition. A direct proof for the deposition of sulfur over graphene layers and the formation of oxygen-sulfur bond are the S2p spectrum, which is shown in Fig. 7 (f) (see also discussion below). The

reduction of the peaks related to oxygen bound to C after sulfur impregnation is also reflected in the relative oxygen concentrations within the sample surfaces of S-*rGO* (~10.4 atomic-%) and *rGO* (~12 atomic-%), which were derived from the quantitative analysis of the detail spectra. Recent reports had shown that C-S bond formation during sulfur impregnation over GO can reduce the oxygen content within GO.[28]

The electrochemical studies of Mg/S rechargeable battery system were carried out by building Swagelok type cells with S-*rGO* as cathode material and Mg-carbon composite (80:20 % w/w, prepared by ball milling) as anode material. The sulfur loading within the cathode electrode was 1.5 mg cm^{-2}. 80 µL of non-nucleophilic electrolyte was used for each cell. The electrolyte was prepared by mixing a non-nucleophilic base of magnesium-bis(hexamethyldisilazide) [(HMDS)$_2$Mg] with the Lewis acid, AlCl$_3$ (1:2 molar ratio) and dissolving the reaction product in a tetraglyme (C$_{10}$H$_{22}$O$_5$) ethereal solvent according to chemical reaction (1).[7]

$$2[(HMDS)_2Mg] + 4AlCl_3 \Leftrightarrow [Mg_2Cl_3][(HMDS)AlCl_3] + 3[(HMDS)AlCl_2] \dots\dots \quad (1)$$

$$[(HMDS)AlCl_2] + 2MgCl_2 \Leftrightarrow [Mg_2Cl_3] [(HMDS)AlCl_3] \dots\dots\dots\dots\dots (2)$$
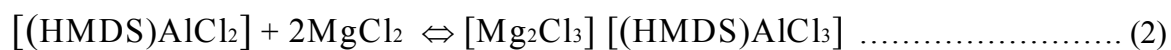
[Mg$_2$Cl$_3$]$^+$[(HMDS)AlCl$_3$]$^-$ is the electrochemically active complex, while [(HMDS)AlCl$_2$] is a neutral by-product. To also convert the neutral [(HMDS)AlCl$_2$] by-product into the electrochemically active complex [Mg$_2$Cl$_3$]$^+$[(HMDS)AlCl$_3$]$^-$ according to reaction (2), MgCl$_2$ was slowly added to the solution attained by the chemical reaction (1). Thus, the Mg ion concentration could be increased up to 1.8 M. Recent studies in a Li/S battery show that polysulfide dissolution to the anode side can be suppressed by increasing the viscosity of

electrolyte solution and enhancing the lithium ion concentration within electrolyte.[7, 29] Inconel 625 was used as the current collectors, which show good corrosion resistance against the chloride containing electrolyte.[30] Cyclic voltammetry (CV) measurements were carried out (Fig. S3: supporting information) to determine the electrochemical window of the electrolyte using a two-electrode cell containing a Inconel disc as the working electrode and Mg as the reference and counter electrode. The CV shows the reversible Mg deposition capability and a voltage stability of the electrolyte up to 3.2 V.

Fig. 8 (a) depicts the first cycle galvanostatic discharge/charge curve of Mg/S rechargeable battery with S-*rGO* as cathode and Mg-carbon composite as anode electrodes, at the current density of 20 mA g^{-1} and voltage in the range 0.5 - 2.5 V. The capacity values were calculated based on the mass of sulfur at the cathode electrode. The open circuit voltage (OCV) for the fresh cell was stabilized at 1.72 V after 12 hours resting time. The S-*rGO* nanocomposite delivered a high initial discharge capacity of 1024 mAh g^{-1} and a charge capacity of 548 mAh g^{-1}. During the second cycle, the cell gave a discharge and charge capacity of 448 mAh g^{-1} and 396 mAh g^{-1}, respectively. The first discharge voltage profile of Mg/S cell showed two voltage plateaus similar to Li/S cell.[31, 32] The first small plateau in the voltage profile was between 1.72 and 1.3 V and the second plateau was within the range of 1.3 – 0.7 V. During the discharge, the sulfur within the S-*rGO* cathode electrode passes through several distinct reductive steps: in the first step, there is a reduction of the solid cyclo-S_8 to S_8^{2-} via the formation of liquid polysulfide (PS) MgS_8, which is subsequently reduced to the PS, MgS_6 and then to MgS_4.[7, 33] Since these polysulfides may be soluble within the electrolyte, the reaction kinetics is fast, which gives the first small voltage plateau with a capacity contribution of ~ 186 mAh g^{-1} in the discharge curve. In the following reductive

steps, liquid MgS_4 polysulfide is reduced to solid MgS_2 and that gives a second voltage plateau with a capacity contribution of ~ 700 mAh g^{-1} in the discharge curve. In the final step, MgS_2 is reduced to MgS, which represents the tail in discharge voltage profile. Since the electrochemical reactions at the second plateau and tail of the voltage profiles are more sluggish, the reaction is slowed down and it is difficult to attain the theoretical capacity (~ 1675 mAh g^{-1}) of the MgS cell.[1, 7] The overall electrochemical reactions within the Mg/S battery can be represented by the following equations (3), (4) and (5).[7, 33]

$$S_8 + 4e^- + 2Mg^{2+} \rightarrow 2MgS_4 \qquad \text{------------------------------ (3)}$$

$$MgS_4 + 2e^- + Mg^{2+} \rightarrow 2MgS_2 \qquad \text{------------------------------ (4)}$$

$$MgS_2 + 2e^- + Mg^{2+} \rightarrow 2MgS \qquad \text{------------------------------ (5)}$$

The discharge/charge curves for the 2nd, 3rd and 4th cycles are illustrated in Fig. 8 (b). The discharge/charge capacities for the initial and final cycles are given in Table 1 and which show a major decrease in the capacity from the first to second discharge. From the second discharge onwards, a drop off in the capacity contribution from the first voltage plateau and a merging of first and second voltage plateau was noticed in the discharge curve. This could be due to MgS/MgS_2, which are forming after first discharge and seem to not convert back completely into elemental sulfur in the later cycles. Thus, a certain amount of high-order Mg polysulfides could remain at the end of charging, similar to Li/S battery.[10] Hence, after the first cycle, the cathode and electrolyte may contain different higher order polysulfides from

MgS$_8$ to MgS$_4$. The cyclic stability data (Fig. 9 (a)) show a capacity fading for the initial cycles similar to what was observed in the Li/S battery system, mainly due to the presence of some sulfur within the cathode, which is going through an irreversible transformation-dissolution process.[34-36] Afterwards, relatively stable cyclic stability has been observed for further 50 cycles (See Table 1 and Fig. 9 (a)). At the end of 6th cycle, the discharge and charge capacity values were 280 mAh g^{-1} and 279 mAh g^{-1}, respectively. From the 7th cycle onward, the charge capacity contribution gradually increased as compared to the corresponding discharge capacity. The increase of charge capacity over the discharge capacity after some initial cycles is probably due to Mg polysulfide shuttle effect, which acts as a parasitic side reaction. At the end of 50th cycle, the discharge and charge capacity values were 219 mAh g^{-1} and 236 mAh g^{-1}, respectively. The current rate capability of S-*rGO* cathode material in Mg/S battery was investigated after running the cell for initial 10 cycles at the current density of 20 mA g^{-1} and the corresponding discharge/charge voltage profiles are given in Fig. 9 (b). The discharge capacities for different current rates are summarized in Table 2. The voltage profiles show that both discharge voltage plateaus and the capacity decrease gradually with increasing current rate, which may be attributed to higher ohmic and kinetic overvoltage at higher current rate and sluggish kinetics of Mg with S.[8, 37]

In comparison with previous results on Mg/S batteries, the present results show a progress. Muldoon *et al*. tested a Mg/S battery for the initial two cycles with first and second discharge capacities of 1200 mAh g^{-1} and 394 mAh g^{-1}, respectively, the voltage plateau was below 0.9 V.[1] The authors observed a clearly visible yellow discolouration of the separator as result of polysulfide dissolution that contributes to capacity fading. During the first discharge of this cell, the voltage plateau increased from 0.55 V to 0.89 V due to the breaking of a resistive

surface layer on the metallic magnesium anode electrode. In a recent study, Zhao-Karger *et al*. could improve the performance of a Mg/S cell using sulfur loaded poly(ethylene glycol) functionalized mesoporous carbon material (CMK-3) as cathode electrode along with a non-nucleophilic electrolyte in glyme/ionic liquid solutions.[7] Using the same combination of electrolyte and binder as in our present study, the first discharge capacity of this Mg/S cell was 500 mAh g^{-1} (current density of 20 mA g^{-1}) with an initial voltage plateau of about 1.65 V. The authors could run the cell for the initial 20 cycles with a final discharge capacity of 260 mAh g^{-1}. In another report, Ha *et al*. presented a Mg/S cell with a first discharge capacity of 500 mAh g^{-1} and a voltage plateau of 0.2 V using 0.3 M Mg(TFSI)$_2$ in a glyme/diglyme mixed solvent electrolyte.[38]

To get more insight into the battery reaction mechanism, XPS measurements were carried out for the S-*rGO* cathode (Fig. 7(e-f)) and the Mg/C anode (Fig. S4: Supporting Information) electrodes after battery cycling in the discharged state. For this purpose, the cells were disassembled in an argon filled glove box. The electrodes were separated, rinsed with anhydrous tetraglyme to remove the electrolyte residues and dried in vacuum. Subsequently, the electrodes were placed in an inert gas filled chamber and transferred into the XPS vacuum chamber. Fig. 7 (e) depicts the XP survey spectrum of the S-*rGO* cathode after the 50th discharge, which shows the peaks corresponding to Mg such as Mg 1s (1304.0 eV), Mg 2s (89.3 eV) and Mg 2p (50.5 eV), mainly coming from the formation of MgS$_x$. The additional peaks corresponding to fluorine and chlorine within the survey spectrum can be attributed to the binder and some residues of electrolyte. The inset of Fig. 7 (e) shows the high resolution

Mg 1s XP spectrum. Fig. 7 (f) compares S2p XP spectra of the S-*rGO* cathode electrode before battery cycling and after the 50th cycle in the discharged state. The S2p spectrum of the fresh S-*rGO* cathode electrode can be deconvoluted into two peak couples. The first one, with peaks at 163.8 and 165.0 eV corresponds to the S $2p_{3/2}$ and S $2p_{1/2}$ doublet of elemental sulfur, the smaller peak couple at 168.4 and 169.6 eV can be ascribed to the bond formation between sulfur and oxygen functional groups present over the *rGO* surfaces (SO$_x$), as was already seen in the O(1s) detail spectrum and in FTIR measurements also. After the 50th discharge, a shift of the first peak doublet to lower BE is obvious (now 162.7 and 163.9 eV), this shift confirms the formation of MgS$_x$ ($1 < x < 8$), which was also reported earlier.[1, 7, 39] The peak couple at higher BE is attributed to higher oxidation states of sulfur again, i.e., SO$_x$ bond and MgSO$_y$ containing S-O and S=O bonds.[40] The analysis of the XP spectra of the Mg/C anode electrode after the 50th discharge (Fig. S5: supporting information) shows a small but detectable amount (~ 0.6 %) of sulfur in the form of Mg polysulfides (MgS$_x$).

The important role of rGO as a host matrix for sulfur active material towards battery performance was further confirmed by testing the battery performances of a pure sulfur cathode without rGO (Fig. S5: supporting information) using the same cathode sulfur loading (1.5 mg cm^{-2}) and amount of electrolyte (80 µL). The cell shows a drastic capacity fading from the first discharge (111 mAh g^{-1}) to 3rd discharge (2 mAh g^{-1}) and failure of the battery for further cycles. This shows clearly that a good porous and conductive host matrix is necessary to cycle a sulfur cathode material, also in Mg/S rechargeable battery. The influence of oxygen functional groups over rGO towards electrochemical battery performance was evaluated by comparing to rGO material from which part of the oxygen functional groups were removed. For this purpose, the as prepared rGO was further heat treated to high

temperature (900 °C) under vacuum. The FTIR spectrum of this material (Fig. S1: supporting information) shows that the majority of oxygen functional groups were removed from the rGO sample after this treatment. Using this material, Sulfur-rGO (900 °C) composite was prepared by mechanical mixing and the Mg/S cell performances of it was tested under the same experimental conditions (1.5 mg_{sulfur} cm^{-2}, 80 μL electrolyte). The first and second discharge capacities for the cell were 479 and 249 mAh g^{-1} (Fig. S6: supporting information), respectively, with low voltage plateau (~ 0.7 V). After 15 cycles, the discharge capacity had dropped to 71 mAh g^{-1}, while it was 228 mAh g^{-1} for the S-rGO cathode composite (cf. Table 1). This performance degradation of S-rGO (900 °C) as compared to S-rGO cathode indicates the importance of (i) a highly porous morphology of structure, and (2) the presence of oxygen functional groups over the support for strong adsorption of sulfur and further forming Mg polysulfides with the graphene layers during battery cycling.

The Mg/S cell with sulfur dispersed *r*GO as cathode electrode gives good cyclability and a better current rate capability due to the special functional and morphological properties of reduced graphene oxide.[1, 41] The corresponding electrochemical mechanism has been given in the schematic Fig.10. The two dimensional, large surface area and porous morphology of *rGO* gives more adsorption sites for the dispersion of sulfur and acts as a buffer layer to accommodate the volume changes during the insertion or extraction of Mg into sulfur active material in charging/discharging.[42, 43] In addition, the oxygen functional groups present over the surface of *rGO,* especially carbonyl, epoxy and hydroxyl groups, can bond with sulfur particles and immobilize them and the later formed Mg polysulfides.[25, 44] The uniform

dispersion of the sulfur particles over the surface of conductive *rGO* gives an intimate electronic contact between current collector and insulating sulfur active material. Even though the present results of the Mg/S cell using sulfur loaded *r*GO as cathode along with a non-nucleophilic electrolyte are promising, further improvements of the reversible capacity and cyclic stability are required. For these, it is necessary to get a deeper insight into the Mg polysulfide dissolution and bonding formation of Mg polysulfides with different oxygen functional groups.

4. Conclusions

We have developed an Mg/S battery with good cyclability using a graphene based sulfur composite electrode and a non-nucleophilic electrolyte. The cell gives a reversible discharge capacity of 448 mAh g^{-1} and a discharge capacity of 236 mAh g^{-1} at the end of 50th cycle and better current rate capability also. The oxygen functional groups over the surface of *rGO* improve bond formation with sulfur particles and help for uniform dispersion. Along with this, *rGO* acts as a buffer layer, to accommodate the volume changes upon electrochemical cycling between sulfur and MgS, and provides good electronic conductivity and a high surface area for the dispersion of the active material.

Notes

Electronic Supplementary Information (ESI) is available.

Nanoscale Accepted Manuscript

References

1. H. S. Kim, T. S. Arthur, G. D. Allred, J. Zajicek, J. G. Newman, A. E. Rodnyansky, A. G. Oliver, W. C. Boggess and J. Muldoon, *Nat Commun*, 2011, **2**, 427.

2. T. D. Gregory, R. J. Hoffman and R. C. Winterton, *Journal of The Electrochemical Society*, 1990, **137**, 775-780.

3. M. Jäckle and A. Groß, *The Journal of Chemical Physics*, 2014, **141**, 174710

4. X. Ji, K. T. Lee and L. F. Nazar, *Nat Mater*, 2009, **8**, 500-506.

5. O. Tutusaus and R. Mohtadi, *ChemElectroChem*, 2015, **2**, 51-57.

6. Z. Zhao-Karger, X. Zhao, O. Fuhr and M. Fichtner, *RSC Advances*, 2013, **3**, 16330-16335.

7. Z. Zhao-Karger, X. Zhao, D. Wang, T. Diemant, R. J. Behm and M. Fichtner, *Advanced Energy Materials*, 2014, **5**,1401155.

8. P. Saha, M. K. Datta, O. I. Velikokhatnyi, A. Manivannan, D. Alman and P. N. Kumta, *Progress in Materials Science*, 2014, **66**, 1-86.

9. A. Manthiram, Y. Fu and Y.-S. Su, *Accounts of Chemical Research*, 2012, **46**, 1125-1134.

10. D. Moy, A. Manivannan and S. R. Narayanan, *Journal of The Electrochemical Society*, 2015, **162**, A1-A7.

11. Y. V. Mikhaylik and J. R. Akridge, *Journal of The Electrochemical Society*, 2004, **151**, A1969-A1976.

12. Y. Sun, Q. Wu and G. Shi, *Energy & Environmental Science*, 2011, **4**, 1113-1132.

13.   J. Hou, Y. Shao, M. W. Ellis, R. B. Moore and B. Yi, *Physical Chemistry Chemical Physics*, 2011, **13**, 15384-15402.

14.   B. P. Vinayan, N. I. Schwarzburger and M. Fichtner, *Journal of Materials Chemistry A*, 2015, **3**, 6810-6818.

15.   W. S. Hummers and R. E. Offeman, *Journal of the American Chemical Society*, 1958, **80**, 1339-1339.

16.   B. Vinayan, R. Nagar and S. Ramaprabhu, *Journal of Materials Chemistry*, 2012, **22**, 25325-25334.

17.   M. S. Dresselhaus, G. Dresselhaus and M. Hofmann, *Philosophical Transactions of the Royal Society A: Mathematical, Physical and Engineering Sciences*, 2008, **366**, 231-236.

18.   J.-e. Park, Y. J. Jang, Y. J. Kim, M.-s. Song, S. Yoon, D. H. Kim and S.-J. Kim, *Physical Chemistry Chemical Physics*, 2014, **16**, 103-109.

19.   Z.-H. Sheng, L. Shao, J.-J. Chen, W.-J. Bao, F.-B. Wang and X.-H. Xia, *ACS Nano*, 2011, **5**, 4350-4358.

20.   H. Liu, Y. Liu and D. Zhu, *Journal of Materials Chemistry*, 2011, **21**, 3335-3345.

21.   G. Carotenuto, V. Romeo, S. De Nicola and L. Nicolais, *Nanoscale Research Letters*, 2013, **8**, 94.

22.   S. U. Yu, B. Park, Y. Cho, S. Hyun, J. K. Kim and K. S. Kim, *ACS Nano*, 2014, **8**, 8662-8668.

23.   F. Wu, J. Li, Y. Tian, Y. Su, J. Wang, W. Yang, N. Li, S. Chen and L. Bao, *Scientific Reports*, 2015, **5**, 13340.

24. J. Song, T. Xu, M. L. Gordin, P. Zhu, D. Lv, Y.-B. Jiang, Y. Chen, Y. Duan and D. Wang, *Advanced Functional Materials*, 2014, **24**, 1243-1250.

25. L. Ji, M. Rao, H. Zheng, L. Zhang, Y. Li, W. Duan, J. Guo, E. J. Cairns and Y. Zhang, *Journal of the American Chemical Society*, 2011, **133**, 18522-18525.

26. G. Hui, L. Zheng, S. Li, G. Wenhua, G. Wei, C. Lijie, R. Amrita, Q. Weijin, V. Robert and M. A. Pulickel, *Nanotechnology*, 2012, **23**, 275605.

27. H. R. Thomas, A. J. Marsden, M. Walker, N. R. Wilson and J. P. Rourke, *Angewandte Chemie International Edition*, 2014, **53**, 7613-7618.

28. W. Chen, L. Yan and P. R. Bangal, *The Journal of Physical Chemistry C*, 2010, **114**, 19885-19890.

29. E. S. Shin, K. Kim, S. H. Oh and W. I. Cho, *Chemical Communications*, 2013, **49**, 2004-2006.

30. C. Wall, Z.. Zhao-Karger and M. Fichtner, *ECS Electrochemistry Letters*, 2015, **4**, C8-C10.

31. Z. Wang, Y. Dong, H. Li, Z. Zhao, H. Bin Wu, C. Hao, S. Liu, J. Qiu and X. W. Lou, *Nat Commun*, 2014, **5**, 5002.

32. S. Lu, Y. Chen, X. Wu, Z. Wang and Y. Li, *Sci. Rep.*, 2014, **4**, 4629.

33. D.-W. Wang, Q. Zeng, G. Zhou, L. Yin, F. Li, H.-M. Cheng, I. R. Gentle and G. Q. M. Lu, *Journal of Materials Chemistry A*, 2013, **1**, 9382-9394.

34. G. He, X. Ji and L. Nazar, *Energy & Environmental Science*, 2011, **4**, 2878-2883.

35. S. Thieme, J. Bruckner, A. Meier, I. Bauer, K. Gruber, J. Kaspar, A. Helmer, H. Althues, M. Schmuck and S. Kaskel, *Journal of Materials Chemistry A*, 2015, **3**, 3808-3820.

36.   J. Schuster, G. He, B. Mandlmeier, T. Yim, K. T. Lee, T. Bein and L. F. Nazar, *Angewandte Chemie International Edition*, 2012, **51**, 3591-3595.

37.   M. Winter and R. J. Brodd, *Chemical Reviews*, 2004, **104**, 4245-4270.

38.   S.-Y. Ha, Y.-W. Lee, S. W. Woo, B. Koo, J.-S. Kim, J. Cho, K. T. Lee and N.-S. Choi, *ACS Applied Materials & Interfaces*, 2014, **6**, 4063-4073.

39.   R. S. C. Smart, W. M. Skinner and A. R. Gerson, *Surface and Interface Analysis*, 1999, **28**, 101-105.

40.   Y. Diao, K. Xie, S. Xiong and X. Hong, *Journal of The Electrochemical Society*, 2012, **159**, A1816-A1821.

41.   M. Xiao, M. Huang, S. Zeng, D. Han, S. Wang, L. Sun and Y. Meng, *RSC Advances*, 2013, **3**, 4914-4916.

42.   B. P. Vinayan and S. Ramaprabhu, *Journal of Materials Chemistry A*, 2013, **1**, 3865-3871.

43.   J. Jin, Z. Wen, G. Ma, Y. Lu, Y. Cui, M. Wu, X. Liang and X. Wu, *RSC Advances*, 2013, **3**, 2558-2560.

44.   J. W. Kim, J. D. Ocon, D.-W. Park and J. Lee, *Journal of Energy Chemistry*, 2013, **22**, 336-340.

Tables

Table 1: The discharge/charge capacities of S-*rGO* electrode for the initial and final cycles.

Cycle number	Discharge capacity (mAh g^{-1})	Charge capacity (mAh g^{-1})
1	1024	548
2	448	396
3	364	349
4	323	315
5	296	294
6	280	279
7	266	270
10	244	260
15	228	243
50	219	236

Table 2: The discharge capacities of S-*rGO* electrode at different current densities.

Discharge current density (mA g^{-1})	Discharge capacity (mAh g^{-1})
5	885
10	530
15	285
25	180
35	130
45	108

Figures
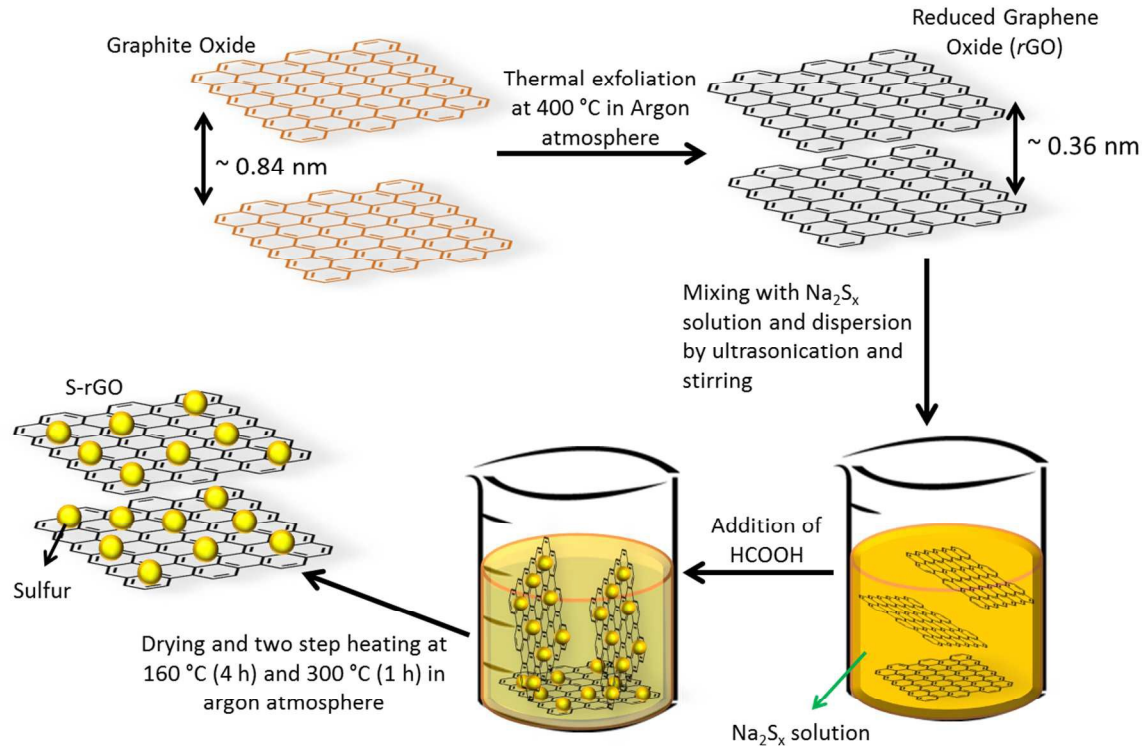
Fig. 1: Schematic diagram of the synthesis procedure adopted for synthesizing graphene based sulfur nanocomposite.
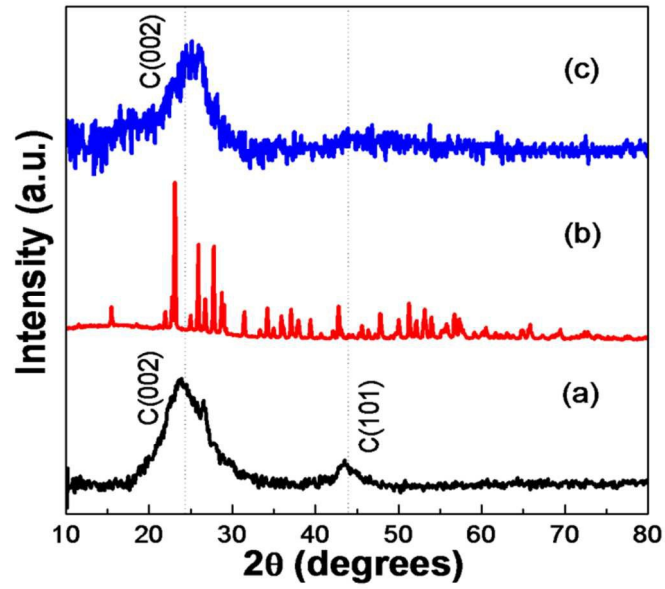
Fig. 2: X-ray diffractograms of (a) *rGO*, (b) Sulfur, and (c) S-*rGO* nanocomposite
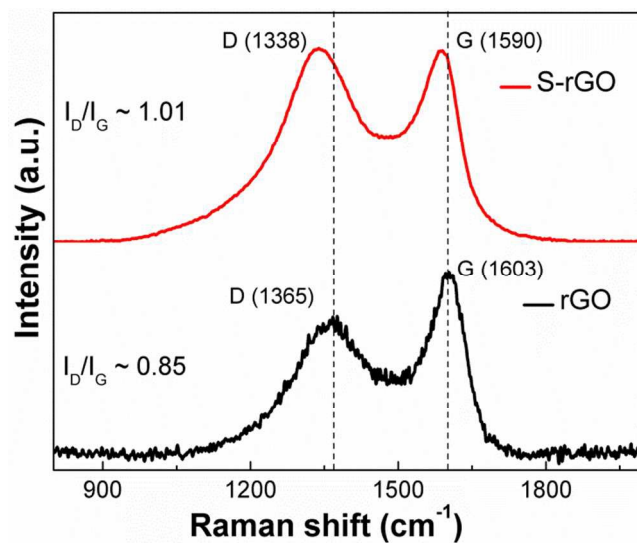
Fig. 3: Raman spectra of *rGO* and S-*rGO* nanocomposite.
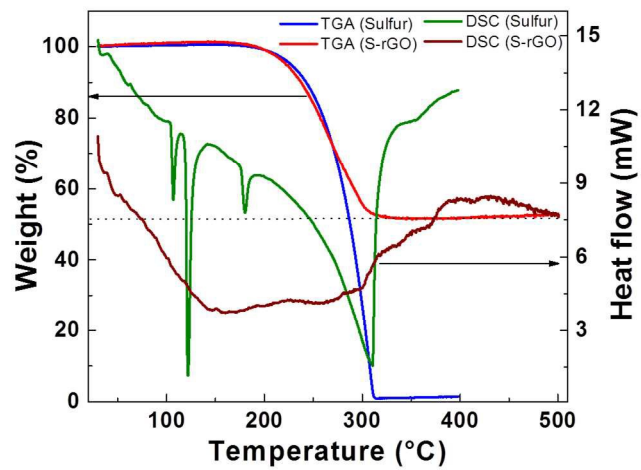
Fig. 4: TGA-DSC analysis of sulfur and S-*rGO* nanocomposite under 20 ml/min helium flow and 10 °C/min heating rate.
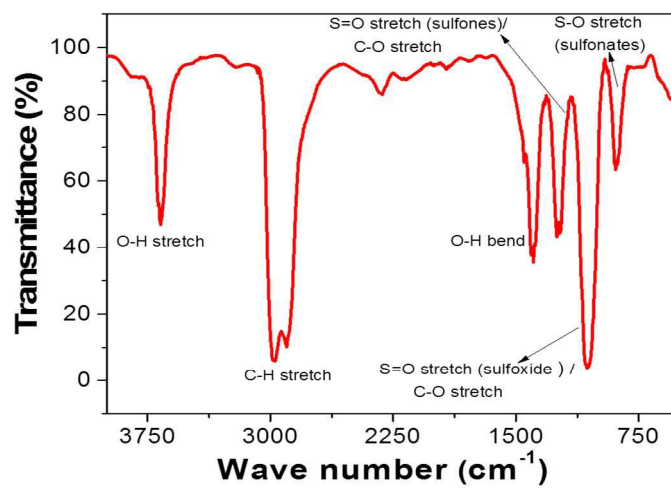
Fig. 5: FTIR spectrum of S-*rGO* nanocomposite.
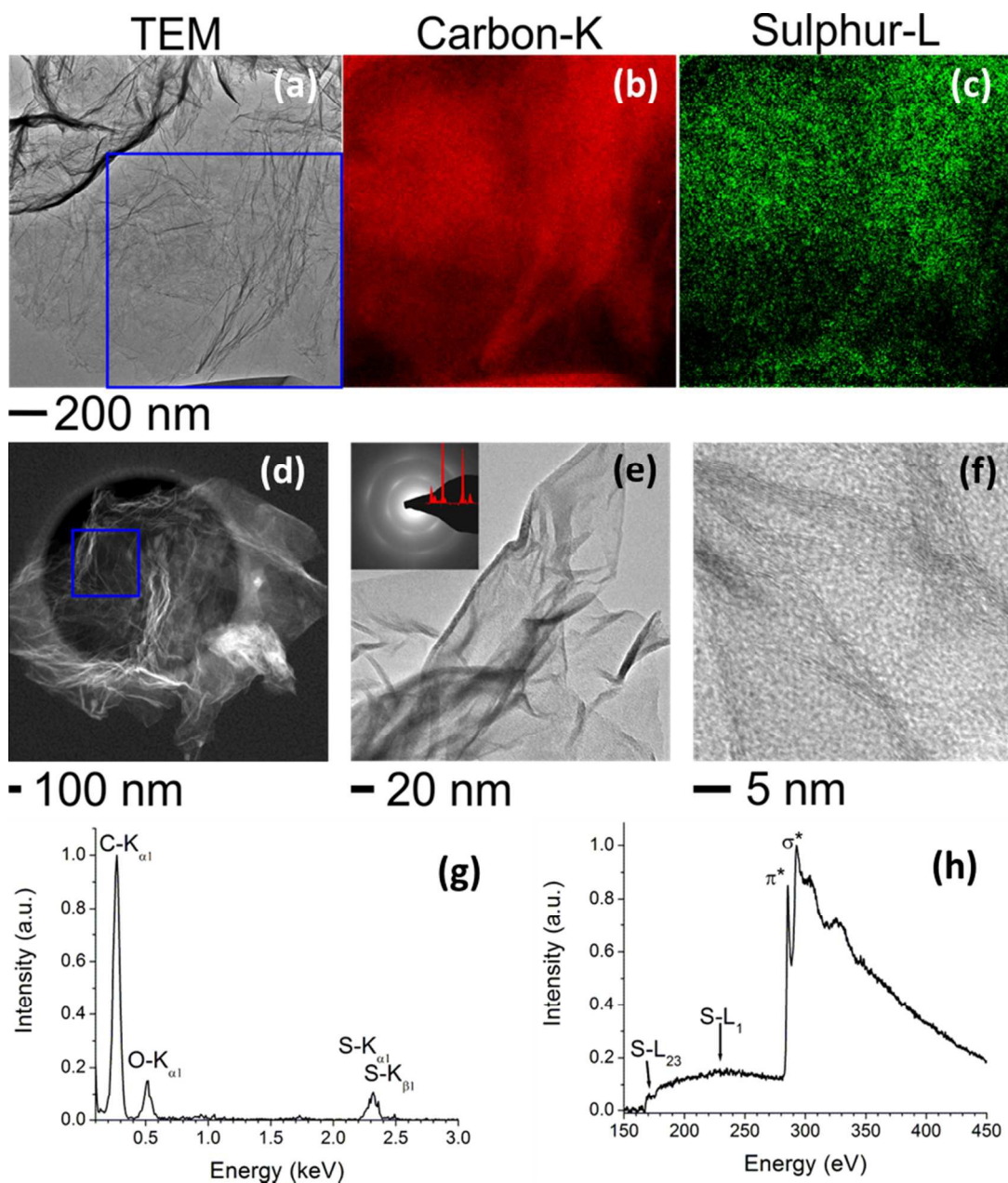
Fig. 6: (a) Bright-field TEM and EFTEM elemental mapping using (b) C-K edge and (c) S-L edges images of the S-rGO. (d) STEM-HAADF image of S-rGO. (e) Bright-field TEM image of S-rGO accompanied with the corresponding indexed SAED pattern, where the measured d-values are 3.54 Å, 2.03 Å, 1.97 Å from the center of the SAED pattern. (f) High resolution TEM micrograph of S-rGO. (g) Energy dispersive X-ray spectrum and (h) electron energy loss spectrum of S-rGO, corresponding to the area marked in the STEM image.
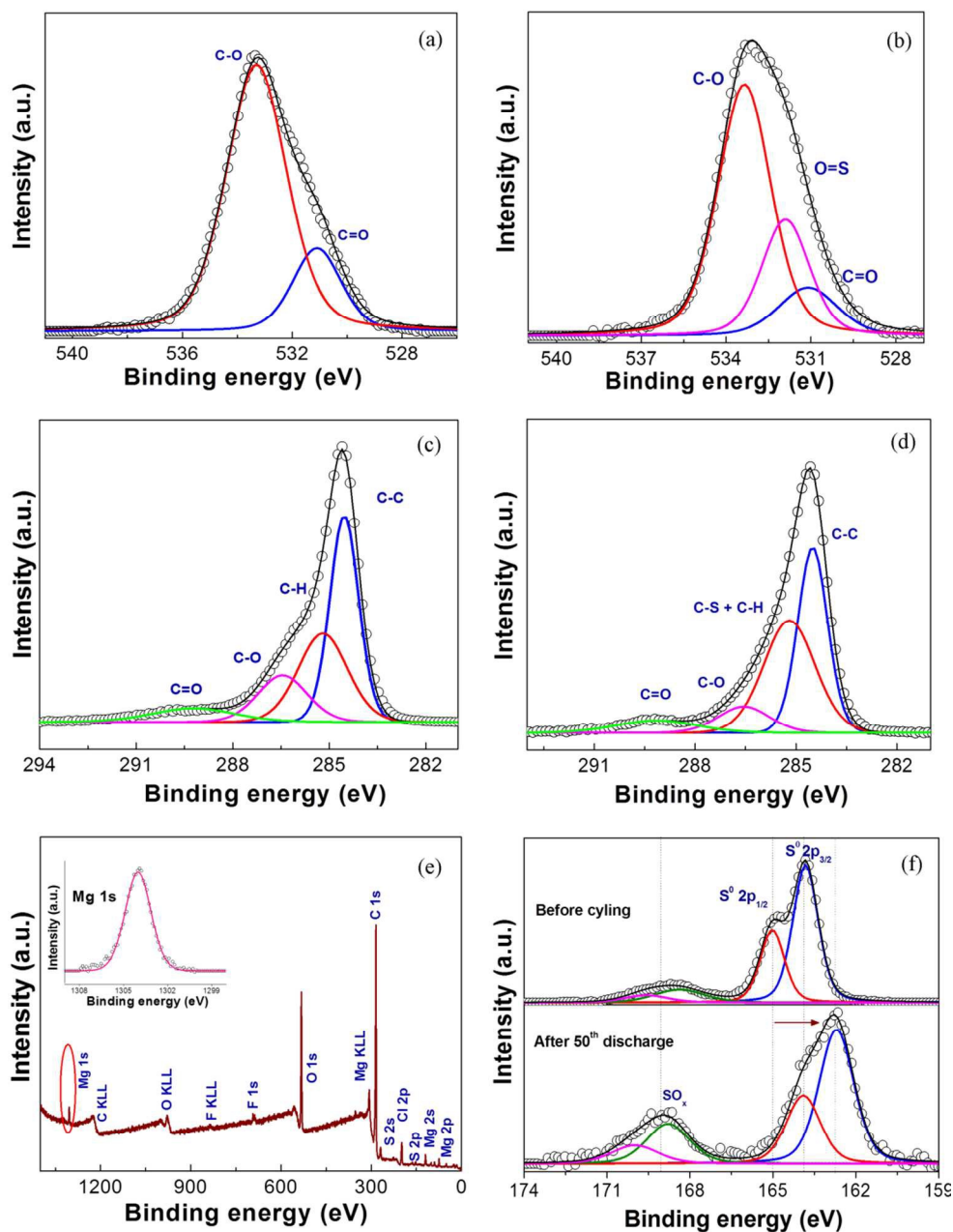
Fig. 7: (a, b) High resolution O1s XPS spectra of *rGO* and S-*rGO*. (c, d) High resolution C1s XPS spectra of *rGO* and S-*rGO*. (e) XPS survey spectrum of S-*rGO* cathode after 50 battery cycles in the discharge state. Inset shows the high resolution Mg 1s XPS spectrum. (f) Comparison of high resolution S2p XPS spectra of S-*rGO* cathode electrode before battery cycling and after 50 cycles in the discharge state.
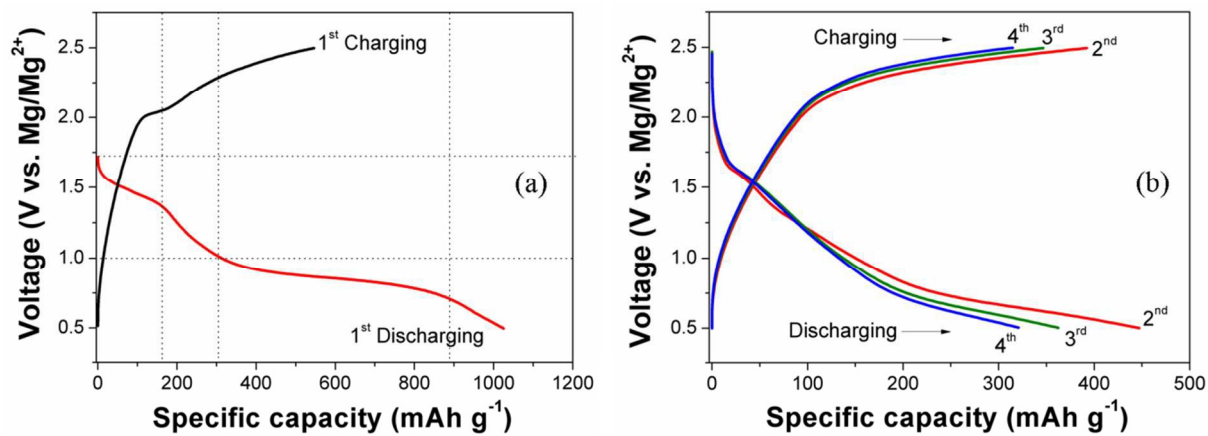
Fig. 8: (a) Initial and (b) 2nd, 3rd and 4th charge-discharge curves of S-*rGO* nanocomposite at a current density of 20 mA g^{-1} in the voltage range of 0.5-2.5 V *vs.* Mg/Mg^{2+}.
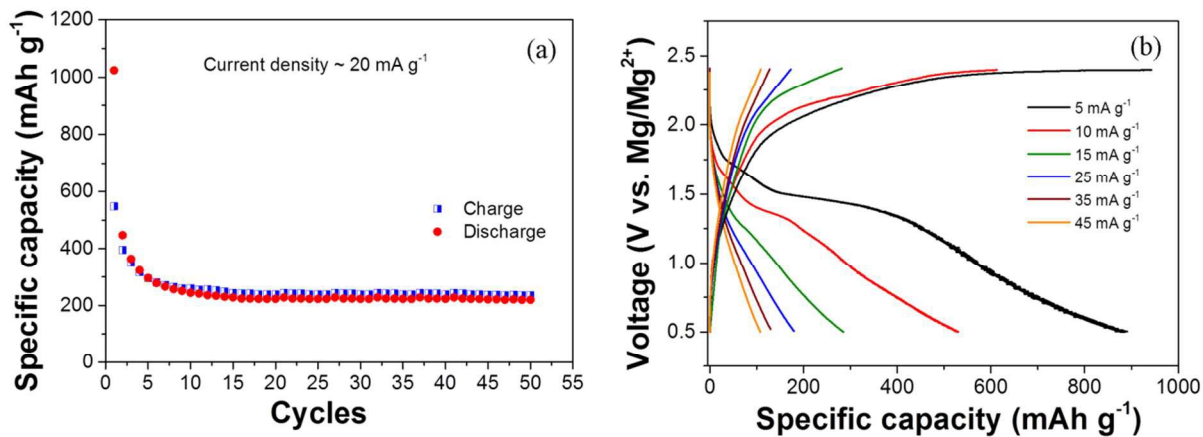
Fig. 9: (a) Cyclic stability of S-*rGO* nanocomposite for the initial 50 cycles at the current density of 20 mA g^{-1}. (b) Current rate capability of S-*rGO* electrode for current densities between 5 and 45 mA g^{-1}.
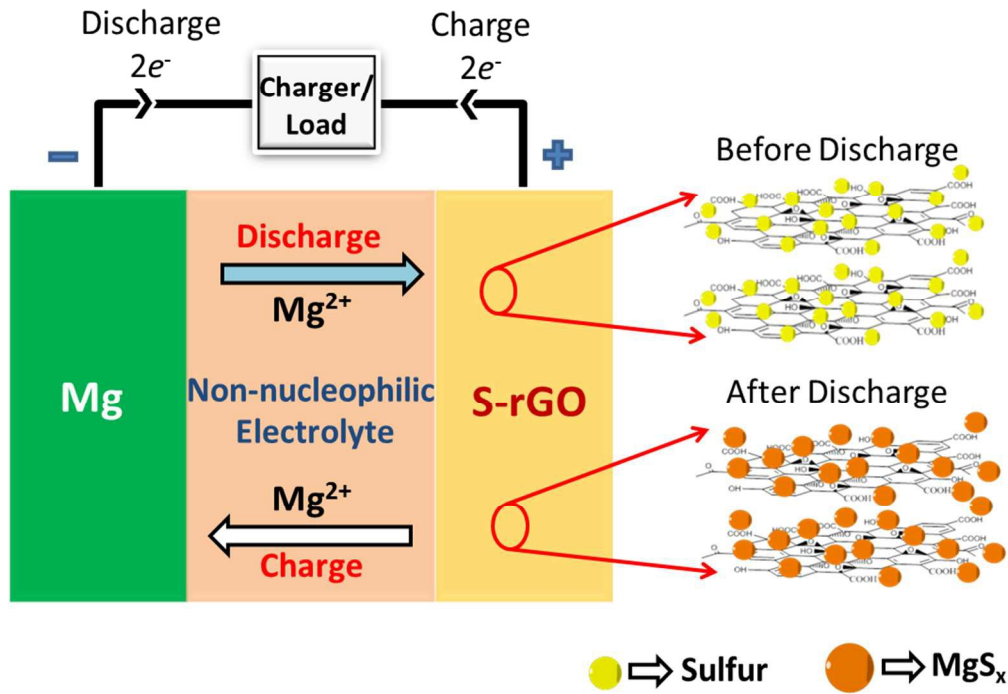
Fig. 10: (a) Electrochemical mechanism of S-rGO nanocomposite electrode within Mg/S cell.